Frontiers of Information Technology & Electronic Engineering
www.jzus.zju.edu.cn; engineering.cae.cn; www.springerlink.com
ISSN 2095-9184 (print); ISSN 2095-9230 (online)
E-mail: jzus@zju.edu.cn



An array of two periodic leaky-wave antennas with sum and difference beam scanning for application in target detection and tracking*

Mianfeng HUANG[1,2], Juhua LIU[†‡1,2]

[1]*School of Electronics and Information Technology, Sun Yat-sen University, Guangzhou 510006, China*

[2]*Guangdong Provincial Key Laboratory of Optoelectronic Information Processing Chips and Systems, Sun Yat-sen University, Guangzhou 510006, China*

[†]E-mail: liujh33@mail.sysu.edu.cn

Received Oct. 16, 2022; Revision accepted Feb. 2, 2023; Crosschecked Mar. 8, 2023

Abstract: An array of two substrate-integrated waveguide (SIW) periodic leaky-wave antennas (LWAs) with sum and difference beam scanning is proposed for application in target detection and tracking. The array is composed of two periodic LWAs with different periods, in which each LWA generates a narrow beam through the n=−1 space harmonic. Due to the two different periods for the two LWAs, two beams with two different directions can be realized, which can be combined into a sum beam when the array is fed in phase or into a difference beam when the array is fed 180° out of phase. The array integrated with 180° hybrid is designed, fabricated, and measured. Measurement results show that the sum beam can reach a gain up to 15.9 dBi and scan from −33.4° to 20.8°. In the scanning range, the direction of the null in the difference beam is consistent with the direction of the sum beam, with the lowest null depth of −40.8 dB. With the excellent performance, the antenna provides an alternative solution with low complexity and low cost for target detection and tracking.

Key words: Antenna; Leaky-wave antenna (LWA); Substrate-integrated waveguide (SIW); Sum and difference beam; Target detection and tracking

https://doi.org/10.1631/FITEE.2200473 **CLC number:** TN82

1 Introduction

Monopulse radar, which uses sum and difference radiation patterns (Milligan, 2005; Mailloux, 2018), is widely applied for detecting and tracking a target accurately. Some radars achieve beam scanning using a mechanical rotating platform, which is bulky and inertial (Hansen RC, 2009). Another technique adopts phased array antennas to accomplish beam scanning quickly and flexibly. However, a phased array antenna requires a complex feed network (Hansen RC, 2009). The leaky-wave antenna (LWA), which can accomplish beam scanning by varying the frequency, can substitute for the phased array antenna to achieve a highly directive beam without a costly feed network (Oliner and Jackson, 2007).

The first leaky-wave structure consists of a slotted rectangular waveguide (Hansen WW, 1946; Oliner and Jackson, 2007), which is bulky and difficult to fabricate. Compared with LWAs based on waveguide, LWAs with the techniques of substrate-integrated waveguide (SIW) (Liu et al., 2012, 2018; Geng et al., 2018; Li YJ and Wang, 2018; Zhou et al., 2018, 2019; Ranjan and Ghosh, 2019; Xu et al.,

‡ Corresponding author

* Project supported in part by the National Natural Science Foundation of China (No. 62171480) and in part by the Guangdong Basic and Applied Basic Research Foundation, China (No. 2020B1515020053)

ORCID: Juhua LIU, https://orcid.org/0000-0003-4725-6241

© Zhejiang University Press 2023

2019; Zhang QL et al., 2019; Rahimi et al., 2021; Singh and Paras, 2022) and microstrip line (Menzel, 1978; Paulotto et al., 2009; Li YX et al., 2010; Williams et al., 2013; Montaseri and Mallahzadeh, 2020; Sarkar et al., 2020; Liu, 2021; Zhang CH et al., 2021; Huang and Liu, 2022; Pan et al., 2022) have attracted more attention due to their low profile, low cost, easy integration, and easy fabrication. The periodic LWA, which typically radiates through its n=−1 space harmonic, is an attractive antenna since it can generate a narrow and directive beam scanning with frequency in the backward and forward quadrants. A periodic LWA usually encounters an open stopband, which has been investigated and suppressed (Paulotto et al., 2009; Li YX et al., 2010; Williams et al., 2013; Liu et al., 2018; Zhou et al., 2018, 2019; Ranjan and Ghosh, 2019; Liu, 2021) for continuous scanning through the broadside.

Some LWAs with dual beams (Xu et al., 2019; Sarkar et al., 2020; Zhang CH et al., 2021; Singh and Paras, 2022) or multiple beams (Geng et al., 2018; Montaseri and Mallahzadeh, 2020; Rahimi et al., 2021; Pan et al., 2022) were proposed. Some LWAs fed by two bidirectional ports were used to synthesize monopulse patterns (Kim and Chang, 2003; Topak et al., 2013; Poveda-García and Gómez-Tornero, 2021; Gil-Martínez et al., 2022b). The bidirectionally-fed patch array was used to realize the monopulse pattern in the broadside direction (Kim and Chang, 2003), and then obtained beam-steering capability using phase shifter and attenuator (Topak et al., 2013). The microstrip LWAs fed by the dual ports were designed to generate the monopulse pattern for direction-of-arrival (DoA) estimation (Poveda-García and Gómez-Tornero, 2021). In addition, monopulse radiation patterns were synthesized for DoA estimation from an array of two half-width microstrip LWAs with four ports (Poveda-García et al., 2019). In Huang and Liu (2022), a microstrip periodic combline LWA with a difference beam scanning was proposed.

In this paper, we propose an array of two SIW periodic LWAs with different periods and integrated with a wideband 180° hybrid. Without any phase shifter, the array can generate a sum pattern and a difference pattern that scan with frequency. The two LWAs have slightly different periods, thereby generating two beams with two slightly different directions. When the array is integrated with a wideband 180° hybrid, the in-phase feed (i.e., Σ-port excitation) can make the two beams merge into a sum beam, whereas the out-of-phase feed (i.e., Δ-port excitation) provides a difference pattern in which the null appears between the two beams. If the two LWAs are with identical periods, a difference pattern that can have its null scanned in the principal plane cannot be obtained. The array with the 180° hybrid is fabricated and measured. The measurement results show that the array with two ports (i.e., Σ-port and Δ-port) can generate a sum pattern and a difference pattern, with the maximum level and the null scanning continuously from the backward to the forward directions. Compared with the conventional mechanical scanning and phased-array scanning antennas, the proposed antenna can realize scanning of sum and difference beams with low cost and low complexity, which can potentially be applied in radar systems for highly accurate target finding and tracking. In addition, with the help of iridescent Internet of Things (IoT) networks, such as Bluetooth, Wi-Fi, or radio frequency identification (RFID) wireless sensor networks, the proposed monopulse LWA can be applied for indoor positioning (Poveda-García et al., 2020; Gil-Martínez et al., 2022a, 2022c; Gómez-Tornero, 2022).

Note that our proposed array contains two LWAs with different periods. Therefore, its pattern is the superposition of the complex far fields of the two scanning beams, in which the information on amplitude and phase is used. This differs from the amplitude-comparison monopulse LWAs, which synthesize the sum and difference patterns using the individual antenna's power patterns (Poveda-García et al., 2019; Gómez-Tornero, 2022; Tamura and Arai, 2022). These amplitude-comparison monopulse LWAs use only the amplitude information and the power-based direction-finding techniques to realize the functionality of angle-of-arrival (AoA) estimation. In the proposed antenna, on the other hand, the phase information is also used to distinguish the direction of the beam (right or left side) for the difference-pattern null. Therefore, the proposed antenna that uses information on the amplitude and phase of the received signals can obtain the monopulse function without ambiguity and estimate the AoA. The proposed array integrated 180° hybrid can realize null scanning when the Δ-port is fed, which also enables it to be used with low-cost

power-based AoA estimation techniques, as proposed previously (Tamura and Arai, 2022).

2 Geometry

The geometry of the periodic LWA is shown in Fig. 1. The SIW is composed of a substrate, which is covered with conductors (i.e., copper) on the top and bottom sides, and it is shorted with two rows of metallic vias at both sides. The proposed array is composed of two such SIW LWAs, having two different modulation periods (i.e., p_1 and p_2). Due to the different periods, the two LWAs with almost the same length may contain different numbers of unit cells, N_1 and N_2. In each LWA, the leakage is from two rows of staggered longitudinal slots, and the radiation is through the n=−1 space harmonic. To suppress the open stopband, two shorting vias are introduced in each unit cell, which are placed opposite to the slots with the centerline (Ranjan and Ghosh, 2019). With two different periods, the two LWAs can generate two beams with different directions. Then, a sum radiation pattern can be generated when the two LWAs are fed in phase, and a difference radiation pattern can be generated when the two LWAs are fed 180° out of phase (through inputs 1 and 2, as shown in Fig. 1a).

To realize the sum and difference beam scanning for the array, a wideband 180° hybrid is demanded. The conventional 180° ring hybrid (Pozar, 2011) works in a narrow band since it provides the phase difference depending on the frequency; so, it is unsuitable for our proposed array. The wideband 180° hybrids proposed earlier (Bialkowski and Wang, 2010; Scherr et al., 2014), which obtain the phase difference by inversion of the electric fields (similar to a magic-T) rather than with different lengths of transmission lines, exhibit wideband features. Moreover, these hybrids (Bialkowski and Wang, 2010; Scherr et al., 2014) have the advantages of easy integration. Therefore, we adopt this type of 180° hybrids (Bialkowski and Wang, 2010) for our array to realize sum and difference beam scanning.

The geometry of the 180° hybrid is shown in Fig. 2, which is modified from the structure proposed in Bialkowski and Wang (2010), for integration into our array. As shown in Fig. 2, port 1, which is fed by a probe, is the Σ-port for generating the in-phase excitations for the array. On the other side, port 2 is the Δ-port for generating the 180° out-of-phase excitations for the array, in which the phase reversal is realized through the slotted ground. We design the 180° hybrid for integration into the array. The widths of the two microstrip lines serving as the feeding lines (inputs 1 and 2 in Fig. 1) for the array should be the same as those for outputs 1 and 2 in Fig. 2. All the relevant parameters for the array are listed in Table 1.

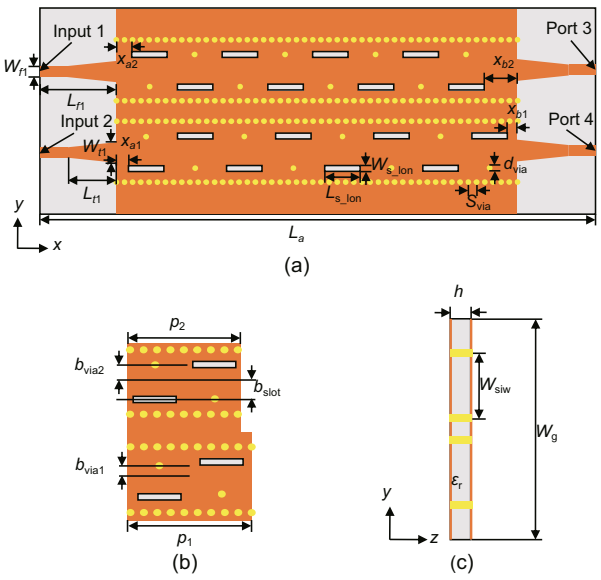


Fig. 1 Geometry of the proposed SIW LWA array: (a) top view; (b) unit cell; (c) cross section (SIW: substrate-integrated waveguide; LWA: leaky-wave antenna)

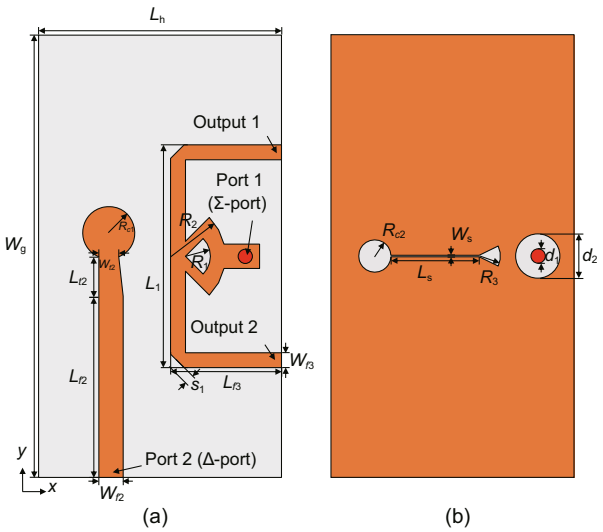


Fig. 2 Geometry of the wideband 180° hybrid: (a) top view; (b) bottom view

Table 1 Parameters and values for the array integrated with 180° hybrid

Parameter	Value	Parameter	Value
W_{f1} (mm)	2.3	W_{g} (mm)	40
L_{f1} (mm)	15	L_{h} (mm)	22
W_{t1} (mm)	4.48	W_{f2} (mm)	2.206
L_{t1} (mm)	10	L_{f2} (mm)	16.388
$W_{\mathrm{s_lon}}$ (mm)	1	W_{t2} (mm)	1.805
$L_{\mathrm{s_lon}}$ (mm)	7	L_{t2} (mm)	3.565
d_{via} (mm)	0.8	R_{c1} (mm)	2.36
S_{via} (mm)	1.5	L_1 (mm)	20.15
L_{a} (mm)	247	R_1 (mm)	4.965
x_{a1} (mm)	3.2	R_2 (mm)	2.265
x_{a2} (mm)	2.2	W_{f3} (mm)	1.35
x_{b1} (mm)	1	L_{f3} (mm)	10.052
x_{b2} (mm)	1	s_1 (mm)	1.224
p_1 (mm)	19.6	R_{c2} (mm)	1.456
p_2 (mm)	18.0	W_{s} (mm)	0.065
b_{slot} (mm)	3.2	L_{s} (mm)	11.35
b_{via1} (mm)	3.2	R_3 (mm)	2.052
b_{via2} (mm)	3.05	d_1 (mm)	1.27
h (mm)	0.762	d_2 (mm)	4
W_{siw} (mm)	12	ε_{r}	2.2
$\tan\delta$	0.0009	N_1	11
N_2	12	L_{all} (mm)	264

3 Antenna design

In this section, we investigate the working mechanism for generating sum and difference patterns using the array of two SIW LWAs with two different periods and thereafter study the 180° hybrid and the array with the hybrid.

3.1 SIW LWAs with two different periods

In this subsection, the two LWAs with two different periodic modulations are studied, and the working mechanism for generating sum and difference radiation patterns is investigated.

As shown in Fig. 1a, suppose that the propagation wavenumbers in the two SIW slotted structures are $k_{x,0,m}=\beta_{0,m}-\mathrm{j}\alpha_m$, where m denotes 1 and 2 for the first and second SIW structures respectively, $\beta_{0,m}$ represents the phase constant of the fundamental space harmonic, and α_m represents the attenuation constant (for the m^{th} SIW structure). Due to the perturbation of the slots with period p_m (for the m^{th} SIW structure), an infinite set of space harmonics is generated, in which the n^{th} space harmonic has the following phase constant:

$$\beta_{n,m}=\beta+\frac{2n\pi}{p_m}. \tag{1}$$

Suppose that the two periodic LWAs are designed such that the radiation beams are contributed by the two $n=-1$ space harmonics. The radiation source for the $n=-1$ space harmonic in the m^{th} LWA can be assumed to be as follows (Huang and Liu, 2022):

$$M_{sm}=A_m\mathrm{e}^{-\mathrm{j}k_{x,-1,m}x}, \tag{2}$$

where A_m is the complex amplitude and $k_{x,-1,m}=\beta_{-1,m}-\mathrm{j}\alpha_m$. Then, the space factor in the scanning plane (x-z plane in the upper half space) can be calculated using the following expression:

$$\begin{aligned}F_m(\theta)&=\int_0^L M_{sm}\mathrm{e}^{\mathrm{j}k_0x\sin\theta}\mathrm{d}x\\&=\int_0^L A_m\mathrm{e}^{-\mathrm{j}k_{x,-1,m}x}\mathrm{e}^{\mathrm{j}k_0x\sin\theta}\mathrm{d}x\\&=A_m\frac{1-\mathrm{e}^{\mathrm{j}k_0L\sin\theta}\mathrm{e}^{-\alpha_mL}\mathrm{e}^{-\mathrm{j}\beta_{-1,m}L}}{\alpha_m+\mathrm{j}\beta_{-1,m}-\mathrm{j}k_0\sin\theta},\end{aligned} \tag{3}$$

where θ represents the angle measured from the z axis.

The radiation angle of the main beam (measured from the broadside direction) for the m^{th} LWA can be determined as follows (Oliner and Jackson, 2007):

$$\sin\theta_m=\beta_m/k_0, \tag{4}$$

where k_0 is the wavenumber in the free space. Then, the space factor for the sum and difference radiation patterns generated by the array of two LWAs in the scanning plane can be calculated as follows:

$$\begin{aligned}F_{\Sigma/\Delta}(\theta)=&\int_0^L(M_{\mathrm{s1}}+M_{\mathrm{s2}})\mathrm{e}^{\mathrm{j}k_0x\sin\theta}\mathrm{d}x\\=&A_1\cdot\left(\frac{1-\mathrm{e}^{\mathrm{j}k_0L\sin\theta}\mathrm{e}^{-\alpha_1L}\mathrm{e}^{-\mathrm{j}\beta_{-1,1}L}}{\alpha_1+\mathrm{j}\beta_{-1,1}-\mathrm{j}k_0\sin\theta}\right.\\&\left.+\rho\cdot\frac{1-\mathrm{e}^{\mathrm{j}k_0L\sin\theta}\mathrm{e}^{-\alpha_2L}\mathrm{e}^{-\mathrm{j}\beta_{-1,2}L}}{\alpha_2+\mathrm{j}\beta_{-1,2}-\mathrm{j}k_0\sin\theta}\right),\end{aligned} \tag{5}$$

where ρ is the ratio of the complex amplitude for the radiation source for the second antenna (A_2) to that for the first antenna (A_1), i.e., $\rho=A_2/A_1$.

Figs. 3a and 3b show the radiation patterns calculated theoretically using Eq. (3) for the two SIW LWAs with periods p_1 and p_2, respectively. Fig. 3c shows the patterns theoretically calculated using Eq. (5) for the array of the two LWAs in the cases of in-phase feed and out-of-phase feed, with the working frequency f=14 GHz. The sum pattern is a pattern that has one main beam, whereas

the difference pattern is a pattern that has two main beams with a null between the two beams, according to Mailloux (2018). With the theoretical calculation, it is found that the values of the complex ratio for generating the sum and difference patterns are $\rho \approx 1 \cdot e^{j180^\circ}$ and $\rho \approx 1 \cdot e^{j0^\circ}$, respectively. The generated difference or sum pattern depends on the superposition of the complex far fields of the two LWAs. In the presented calculation, the propagation wavenumbers are obtained using the data shown in Fig. 4 at 14 GHz, from the simulated data for the SIW LWAs. In any case, however, the phase difference between the excitations for the difference or sum pattern is 180°. To generate a sum (or a difference) pattern with in-phase (or out-of-phase) excitations for the presented array of the LWAs, the two LWAs are placed in an opposite way (Fig. 1a). As shown in Fig. 3c, a sum beam is generated when the array is fed in phase, and a difference beam with a null is generated when it is fed 180° out of phase. The radiation direction of the sum beam coincides with the angle of the null. It is seen that the direction for the sum beam and the null of the difference beam appear at the center of the two main beams of the two single LWAs.

As discussed by Huang and Liu (2022), the null of the difference beam can be calculated approximately as follows:

$$\sin\theta_\Delta \approx \frac{\beta_{-1,1}/k_0 + \beta_{-1,2}/k_0}{2}, \tag{6}$$

where $\beta_{-1,1}$ and $\beta_{-1,2}$ are the phase constants for the n=−1 space harmonics in the two antennas with different periods. Therefore, the direction of the sum beam can also be calculated as follows:

$$\sin\theta_\Sigma \approx \frac{\beta_{-1,1}/k_0 + \beta_{-1,2}/k_0}{2}, \tag{7}$$

due to its coincidence with the null of the difference beam.

Fig. 4 shows the normalized phase and attenuation constants for the two SIW periodic LWAs with different periods p_1 and p_2, which are extracted from the electric fields along the SIW LWAs (Liu et al., 2011). It is seen that the dispersion curves for the SIW LWA with p_1=19.6 mm are shifted to the left compared with those with p_2=18 mm, due to the increase of the period. Similarly, the tuning of dispersion curve was obtained by different widths of the two microstrip LWAs (Poveda-García et al., 2019). This was realized by changing the periods of the two combline LWAs (Huang and Liu, 2022). In the two periodic LWAs, the open stopbands are almost suppressed using the technique described in Ranjan and Ghosh (2019), which can be seen from the attenuation constants that remain almost flat around the broadside frequencies of 13.3 and 14.1 GHz. By adjusting the distance between the slots and the longitudinal centerline, the attenuation constant (α/k_0) can be tuned to provide the desired radiation efficiency. Meanwhile, the detuning of the shifted phase

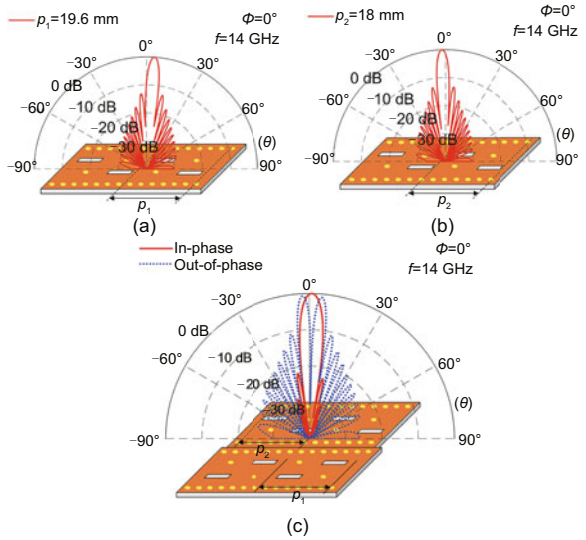


Fig. 3 Radiation patterns calculated using Eq. (3) for the SIW periodic LWAs with p_1 (a) and p_2 (b), and calculated using Eq. (5) for the array with sum and difference radiation patterns (c) (SIW: substrate-integrated waveguide; LWA: leaky-wave antenna)

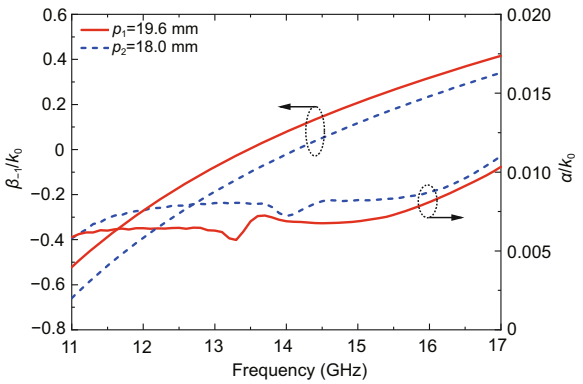


Fig. 4 Normalized phase and attenuation constants for the SIW periodic LWAs with two different periods p_1=19.6 mm (Fig. 3a) and p_2=18.0 mm (Fig. 3b) (SIW: substrate-integrated waveguide; LWA: leaky-wave antenna)

constant (β_{-1}/k_0) curve can be avoided by adjusting the distance between the vias and the longitudinal centerline. Adjusting the distance between the slots and the longitudinal centerline can also lead to the shift of the β_{-1}/k_0 curve. On the other hand, we can also tune the periods of the slot to obtain the desired β_{-1}/k_0 curve.

The array without 180° hybrid is simulated in a high-frequency structure simulator (HFSS) to validate the scanning capability. Fig. 5 shows the angles of the main beams (θ_1 and θ_2) for the two LWAs with periods p_1 (Fig. 3a) and p_2 (Fig. 3b), which are almost consistent with the radiation direction of the first beam and the second beam in the difference beam for the array from the radiation pattern.

Fig. 5 also shows the angles of the sum beam θ_Σ and the null θ_Δ for the array (Fig. 3c). It is seen that the angles of the sum beam θ_Σ and the null θ_Δ from the radiation patterns by HFSS are coincident. In addition, the simulation results agree well with the theoretical ones.

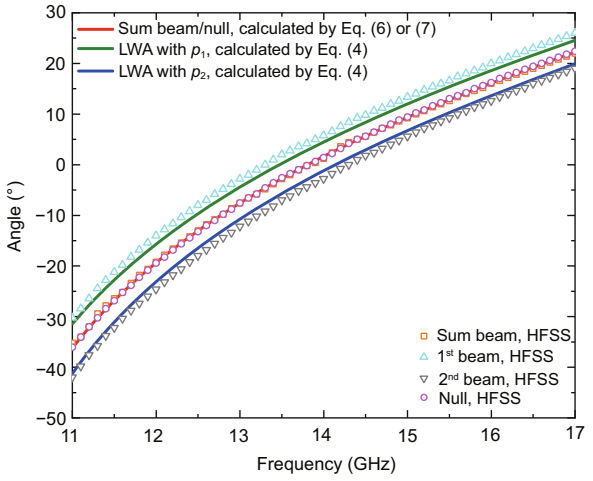


Fig. 5 Angles for the main beams (θ_1 and θ_2) of the SIW LWAs with periods p_1 (Fig. 3a) and p_2 (Fig. 3b) calculated using Eq. (4), the theoretical sum beam/null calculated using Eq. (6) or (7), and the sum beam, first beam, second beam, and null from the simulated radiation pattern (of the array in Fig. 1) (SIW: substrate-integrated waveguide; LWA: leaky-wave antenna; HFSS: high-frequency structure simulator)

3.2 Wideband 180° hybrid

In this subsection, the wideband 180° hybrid is studied and designed for the array of the two LWAs in Section 3.1. The desired band of the hybrid should satisfy the operation band from 11 to 17 GHz for the array in Section 3.1.

Fig. 6 shows the simulated scattering parameters (S-parameters) for the 180° hybrid. In Fig. 6a, the reflection coefficient $|S_{11}|$ for the Σ-port (i.e., port 1) is ≤ -15 dB in the range of 11–17 GHz. In the operation band (from 11 to 17 GHz), the parameter $|S_{21}|$ is ≤ -30 dB, implying an excellent isolation between the Σ-port and Δ-port. The transmission coefficients $|S_{31}|$ and $|S_{41}|$ are about -4 dB and $|S_{31}|$ is almost equal to $|S_{41}|$, implying that the input signal of the Σ-port is equally divided into the two output signals. In Fig. 6b, the reflection coefficient $|S_{22}|$ for the Δ-port (i.e., port 2) is ≤ -12 dB in the range of 11–17 GHz. The parameter $|S_{12}|$ is the same as $|S_{21}|$ due to reciprocity. In the operation band, the transmission coefficients $|S_{32}|$ and $|S_{42}|$ are about -5 dB.

Fig. 7 shows the phase difference between the two output ports (ports 3 and 4) for the 180°

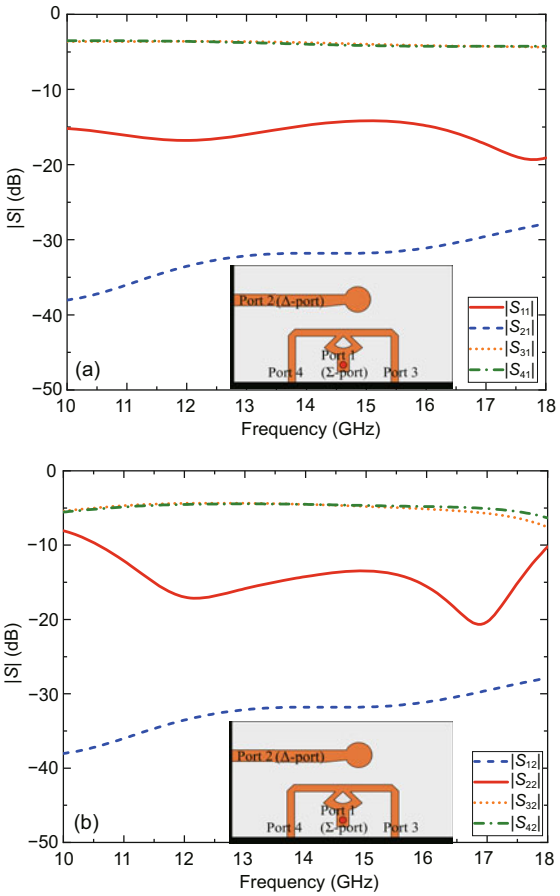


Fig. 6 S-parameters for the wideband 180° hybrid: (a) Σ-port; (b) Δ-port

hybrid. When the Σ-port (port 1) is excited, the phase difference (angle(S_{31}) − angle(S_{41})) is in the range of 0° ± 1.4° in the operation band. When the Δ-port (port 2) is excited, the phase difference (angle(S_{32})–angle(S_{42})) is in the range of 180°±2.9°. The good performance of the wideband 180° hybrid shows that it satisfies the demand for integration into our array (Section 3.1).

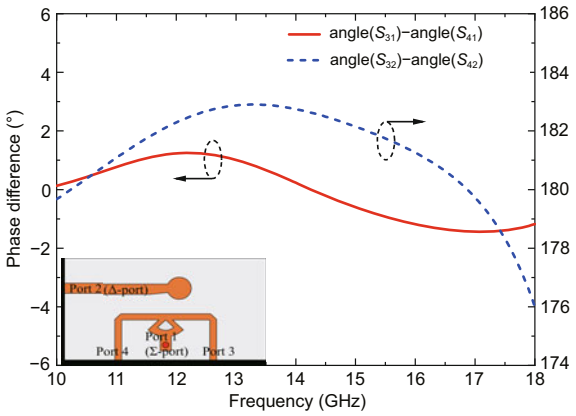


Fig. 7 Phase difference between the two output ports (ports 3 and 4) of the wideband 180° hybrid

3.3 Parameter sweep

In this subsection, the null depth is optimized by studying the array (proposed in Section 3.1) integrated with the 180° hybrid (proposed in Section 3.2). The null depth is defined as the absolute value at the angle of the null in the normalized radiation pattern (Huang and Liu, 2022). The parameters x_{a1} and x_{a2}, which relate to the starting positions of the two rows of the slots, are very important for the null, since they affect the phase difference of the two radiating space harmonics (Huang and Liu, 2022) or the complex ratio ρ in Eq. (5).

Fig. 8 shows the difference radiation patterns calculated using Eq. (4) and simulated by HFSS. It is seen that the simulated difference radiation pattern exhibits a null reaching −31.3 dB at θ_Δ=1.2°, which agrees well with the pattern calculated using Eq. (4), in which the null reaches −30.6 dB at θ_Δ=1.2°.

Fig. 9 shows the effect of the parameters x_{a1} and x_{a2} on the null depth. In Fig. 9a, it is seen that the null depth becomes lower when x_{a1} decreases at relatively low frequencies such as f=11.5, 12.5, and 13.5 GHz. However, the decrease of x_{a1} leads to the deterioration of null performance at relatively high frequencies such as f=15.5 and 16.5 GHz. Therefore, x_{a1} = 3.2 mm is a better choice for the operation band from 11 to 17 GHz. In Fig. 9b, the increase of x_{a2} results in a lower null depth when f=11.5, 12.5, and 13.5 GHz, but the null depth increases when f = 15.5 and 16.5 GHz. Therefore, it is better to choose x_{a2}=2.2 mm.

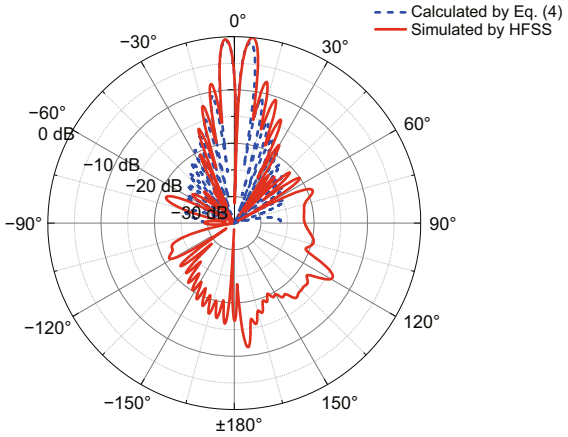


Fig. 8 Difference radiation patterns calculated using Eq. (4) and simulated by HFSS when f = 14 GHz and ϕ = 0° (HFSS: high-frequency structure simulator)

4 Experimental verification

In this section, a prototype of the antenna is fabricated and measured. The top and bottom views of the fabricated antenna are shown in Fig. 10. The antenna is fabricated on a Wangling F4BMX220 substrate, which has a thickness h = 0.762 mm, a relative permittivity ε_r = 2.2, and a loss tangent tan δ=0.0009. The conductor is copper, with a conductivity $\sigma = 5.8 \times 10^7$ S/m. When the antenna is excited by the Σ-port, the antenna generates a sum beam scanning with frequency. When the antenna is excited by the Δ-port, the antenna realizes a difference beam (i.e., null scanning). With either the Σ-port or Δ-port being excited, the other three ports are connected to a 50-Ω load.

The simulated and measured S-parameters are shown in Figs. 11–14. Fig. 11 shows the reflection coefficients for the Σ-port (port 1) and Δ-port (port 2). In the range of 11–17 GHz, the measured and simulated reflection coefficients of the Σ-port and Δ-port are ≤−10 dB. Fig. 12 shows the isolation between the Σ-port and Δ-port. From 11 to 17 GHz, the measured $|S_{21}|$ is ≤−20 dB, which is almost consistent

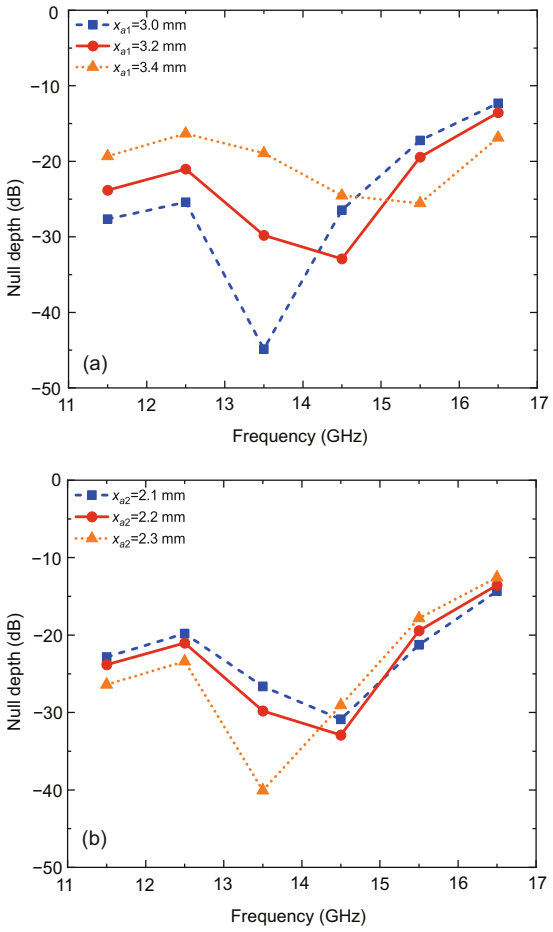


Fig. 9 Null depth for the proposed antenna from the simulation radiation patterns with different values of x_{a1} when $x_{a2}=2.2$ mm (a) and with different values of x_{a2} when $x_{a1}=3.2$ mm (b)

with the simulated one, indicating a good isolation between the Σ-port and Δ-port. Fig. 13 shows the measured and simulated transmission coefficients between the Σ-port and the two output ports (ports 3 and 4). In the operation band, the simulated $|S_{31}|$ and $|S_{41}|$ are about −7 dB, and the measured $|S_{31}|$ and $|S_{41}|$ are about −9.5 dB. The difference between $|S_{31}|$ and $|S_{41}|$ is small. Fig. 14 shows the measured and simulated transmission coefficients between the Δ-port and the two output ports (ports 3 and 4). The simulated $|S_{32}|$ is nearly equal to $|S_{42}|$, and they are about −9 dB. The measured $|S_{32}|$ and $|S_{42}|$ are about −12 dB. Both Figs. 13 and 14 show that the measured transmission coefficients are about 3 dB lower than those from simulation, which is caused by the loss of the SubMiniature version A (SMA) connector and the greater losses of the materials.

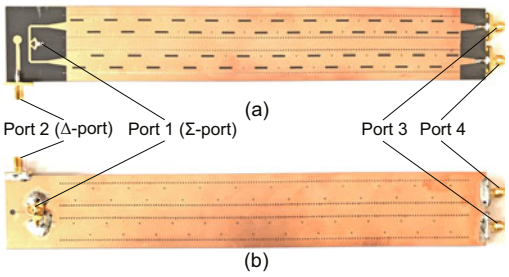


Fig. 10 Array of two periodic LWAs with different periods integrated with the 180° hybrid: (a) top view; (b) bottom view (LWA: leaky-wave antenna)

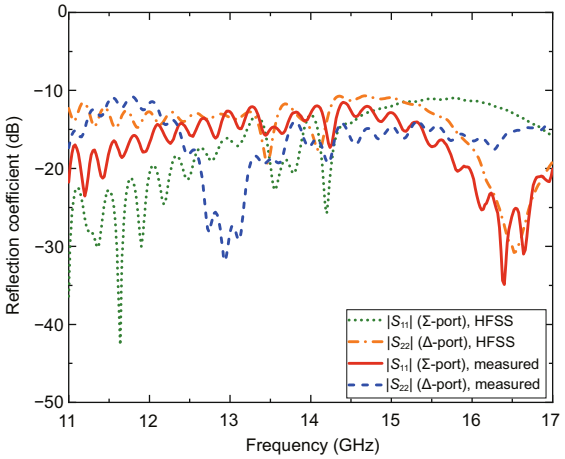


Fig. 11 Simulated and measured reflection coefficients of the Σ-port and Δ-port for the proposed antenna

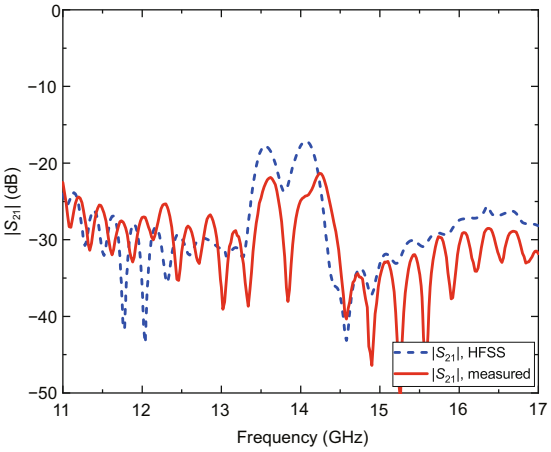


Fig. 12 Simulated and measured isolation between the Σ-port and Δ-port for the proposed antenna

Fig. 15 shows the measured and simulated sum radiation patterns for the proposed antenna at different frequencies (f=11.5, 12.5, 13.5, 14.5, 15.5, and 16.5 GHz) when the Σ-port is excited. At f = 11.5 GHz, the measured radiation direction of the sum beam is at $\theta_\Sigma=-24.6°$, which is very close to the simulated one ($\theta_\Sigma=-26.4°$). When f=13.5 GHz,

the sum beam scans near the broadside, where the simulated sum beam is at $\theta_\Sigma=-2.8°$ and the measured sum beam is at $\theta_\Sigma=-3.4°$. As the frequency increases further, the sum beam scans from the backward quadrant to the forward quadrant. At f=16.5 GHz, the measured radiation direction is at $\theta_\Sigma=17.0°$ and the simulated one is at $\theta_\Sigma=19.0°$. The measurement results for the co-polarization are consistent with the simulation results. The measured cross-polarization is about 5 dB larger than the simulated one, probably because of the fabrication error (it is thought that the cross-polarization is caused by unwanted radiation from the 180° hybrid and the feeding probe of the SMA). A slight difference between the measured radiation direction and the simulated one is observed, due to the dispersion

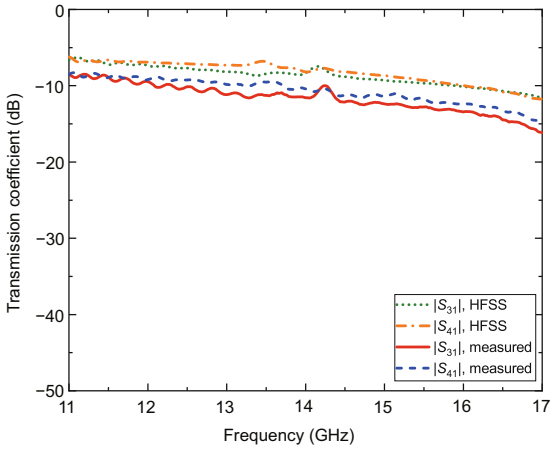


Fig. 13 Simulated and measured transmission coefficients between the Σ-port and the two output ports for the proposed antenna

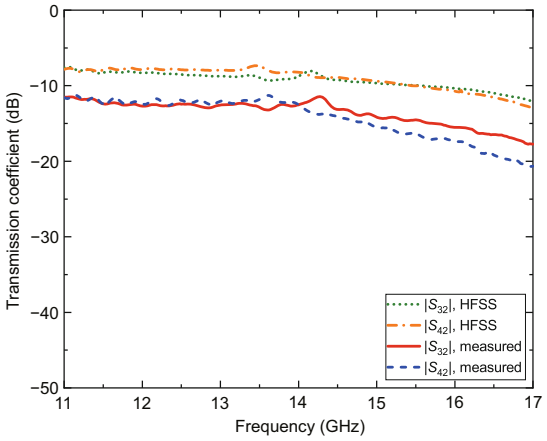


Fig. 14 Simulated and measured transmission coefficients between the Δ-port and the two output ports for the proposed antenna

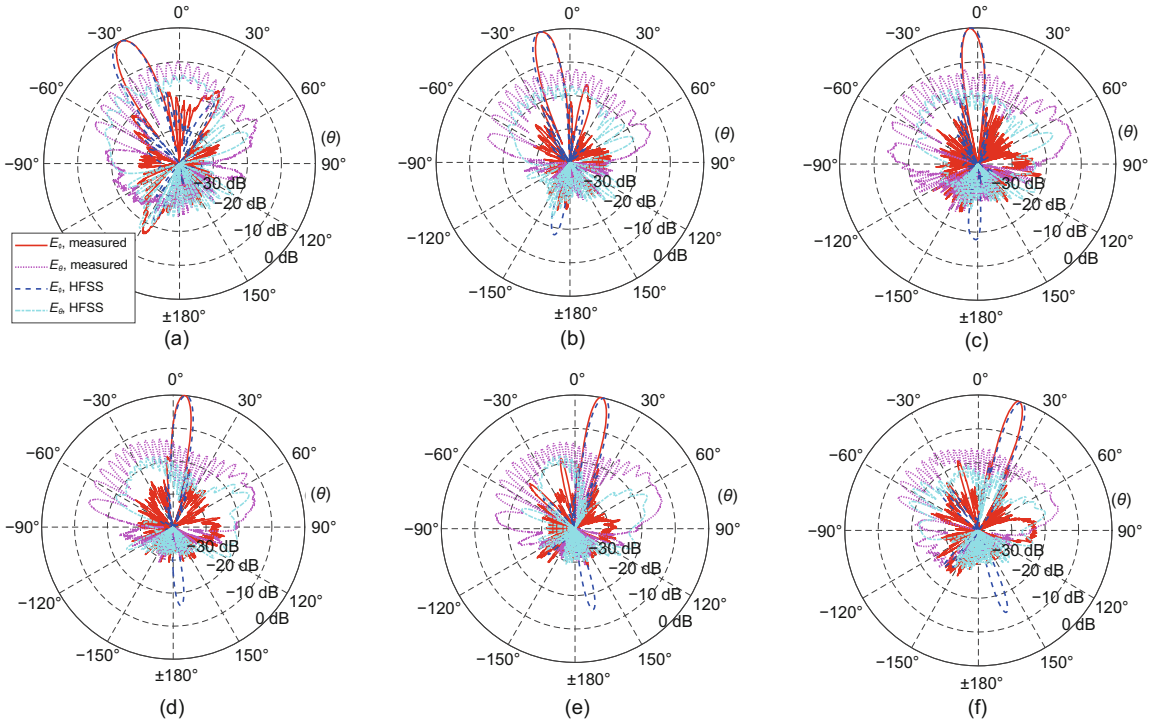


Fig. 15 Sum radiation patterns for the antenna (ϕ=0°): (a) f=11.5 GHz; (b) f=12.5 GHz; (c) f=13.5 GHz; (d) f=14.5 GHz; (e) f=15.5 GHz; (f) f=16.5 GHz

error in the fabricated substrate.

Fig. 16 shows the measured and simulated difference radiation patterns at different frequencies (f=11.5, 12.5, 13.5, 14.5, 15.5, and 16.5 GHz) when the Δ-port is excited. At f=11.5 GHz, the null of the measured difference beam reaches −25.2 dB at θ_Δ=−24.4° and the simulated one reaches −36.8 dB at θ_Δ = −26.8°. The null scanning is consistent with the sum beam scanning in the backward quadrant. As the frequency increases, the angle of the null increases. When the first beam scans near the broadside at f = 13.5 GHz, the measured null reaches −29.9 dB at θ_Δ = −2.2° and the simulated null reaches −42.8 dB at θ_Δ=−2.8°. When the second beam scans near the broadside at f=14.5 GHz, the measured null reaches −25.2 dB at θ_Δ=5.8° and the simulated one reaches −26.5 dB at θ_Δ=5.6°. As the frequency increases further, the null performance becomes worse in the forward direction. The measurement results agree very well with the simulation results.

Fig. 17 shows the measured and simulated realized gains of the sum beam for the antenna. The measured and simulated realized gains of the sum beam increase with the increase of frequency, due to the increase in the electric length (the antenna length over the free-space wavelength). It is seen that the measured gain is very close to the simulated gain in the operation band from 11 to 17 GHz. The measurement and simulation results show that the sum beam of the proposed antenna has a high gain up to about 15.9 dBi.

Fig. 18 shows the measured and simulated realized gains of the difference beam for the antenna. It is seen that the measured and simulated gains are about 12 dBi. In addition, both the measurement and simulation results show that the difference of the gains between the two beams is ≤1 dB, revealing a good balance between the two beams.

Fig. 19 shows the measured and simulated null depths of the difference radiation pattern. The measured null depth is ≤−20.0 dB from 11.0 to 15.5 GHz and the simulated null depth is ≤−20.0 dB from 11.0 to 15.2 GHz. The measured lowest null depth is −40.8 dB at 12.5 GHz and the simulated lowest null depth is −42.8 dB at 13.5 GHz. The measurement and simulation results show that the null depth becomes higher with the increase of frequency when the

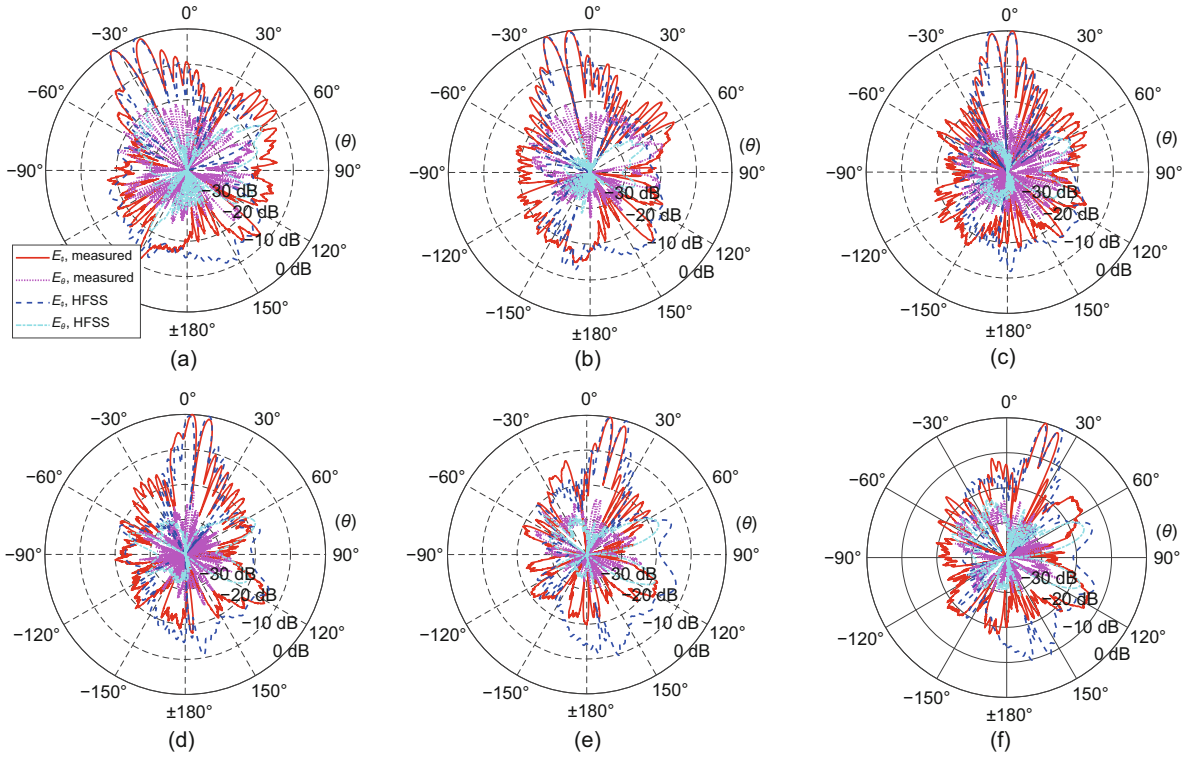


Fig. 16 Difference radiation patterns for the antenna (ϕ = 0°): (a) f = 11.5 GHz; (b) f = 12.5 GHz; (c) f=13.5 GHz; (d) f=14.5 GHz; (e) f=15.5 GHz; (f) f=16.5 GHz

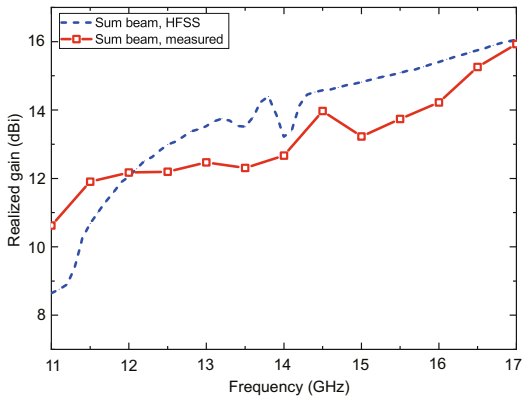


Fig. 17 Simulated and measured realized gains of the sum beam for the proposed antenna

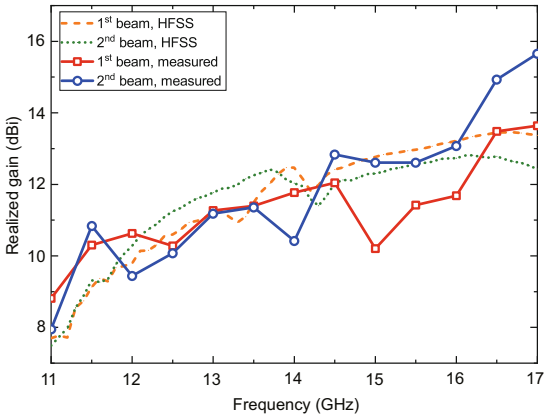


Fig. 18 Simulated and measured realized gains of the first beam and the second beam in the difference pattern for the proposed antenna

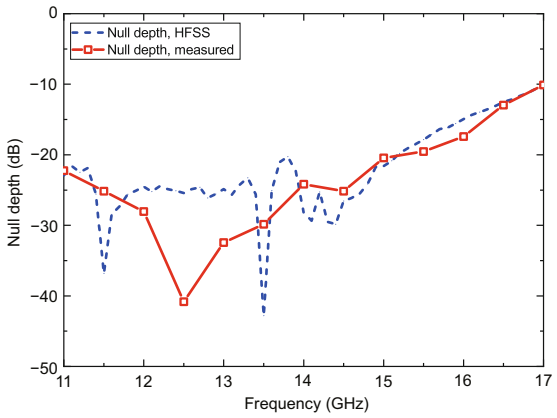


Fig. 19 Simulated and measured null depths for the proposed antenna

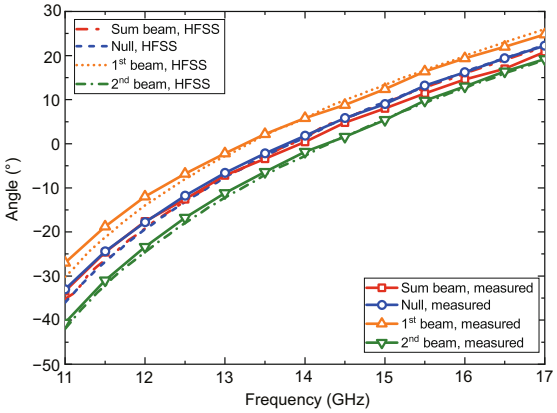


Fig. 20 Angles of the sum beam, null, first beam, and second beam from the simulated and measured radiation patterns

frequency is ≥15 GHz. The low null depth (shown in Fig. 19) and the small difference between the two beams (shown in Fig. 18) demonstrate the excellent performance of the difference beam.

Fig. 20 shows the angles of the sum beam, null, first beam, and second beam from the measured and simulated radiation patterns. The measured sum beam scans from −33.4° to 20.8°, and the simulated one scans from −35.2° to 22.0°. In the difference beam, the measured null that appears between the two beams in the difference pattern scans from −33.0° to 22.0°, which is close to the simulated null that scans from −36.0° to 22.4°. The measurement and simulation results show that the radiation direction of the sum beam and the angle of the null in the difference beam are very close.

For the LWA, the leakage efficiency (power leaked into space divided by total power into the antenna) can be estimated using the following expression:

$$\begin{aligned}\eta_{\text{leakage}} &= 1-\mathrm{e}^{-2\alpha L}\\ &= 1-\mathrm{e}^{-4\pi(\alpha/k_0)(L/\lambda_0)}.\end{aligned} \tag{8}$$

Eq. (8) ignores the dissipative losses in the structure. Because the two LWAs in the array are only with slightly different periods, the attenuation constants (shown in Fig. 4) for the two LWAs are approximately equal. Moreover, the power fed into the two LWAs is approximately equal. The leakage efficiency for the designed array can be estimated approximately by the average of the leakage efficiency of the two LWAs. Fig. 21 shows the leakage efficiency (η_{leakage}) calculated using Eq. (8) for the proposed array in the operation band.

From the perspective of power, the radiation efficiency can be written as follows:

$$\eta_{\text{r}} = \frac{P_{\text{rad}}}{P_{\text{rad}}+P_{\text{C-loss}}+P_{\text{D-loss}}}, \tag{9}$$

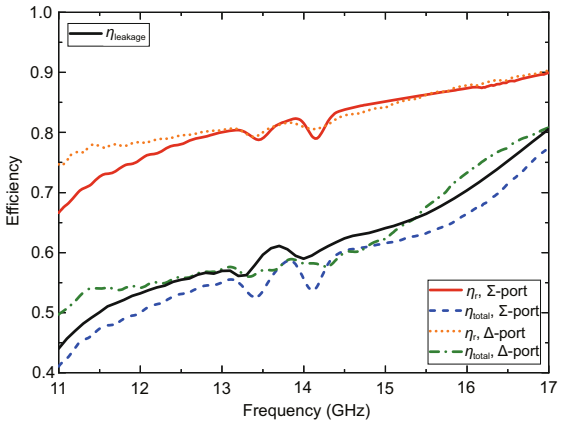


Fig. 21 Leakage efficiency ($\eta_{leakage}$), radiation efficiency (η_r), and total efficiency (η_{total}) for the proposed antenna

where P_{rad} is the radiation power of the antenna, P_{C-loss} is the conductor loss power, and P_{D-loss} is the dielectric loss power. The radiation efficiency is the ratio of the power radiated by the antenna to the power that the antenna consumes, and the total efficiency takes the loss of each port into account further, i.e.,

$$\begin{aligned}\eta_{total} =& \frac{P_{rad}}{P_{all}} \\ =& \frac{P_{rad}}{P_{rad}+P_{C-loss}+P_{D-loss}} \\ &\cdot\left(1-|S_{ii}|^2-\sum_{j\neq i}|S_{ji}|^2\right).\end{aligned} \tag{10}$$

When the Σ-port of the designed antenna is fed, the total efficiency can be written as follows:

$$\begin{aligned}\eta_{total} =& \frac{P_{rad}}{P_{rad}+P_{C-loss}+P_{D-loss}} \\ &\cdot\left(1-|S_{11}|^2-|S_{21}|^2-|S_{31}|^2-|S_{41}|^2\right).\end{aligned} \tag{11}$$

When the Δ-port is fed, the total efficiency is represented as follows:

$$\begin{aligned}\eta_{total} =& \frac{P_{rad}}{P_{rad}+P_{C-loss}+P_{D-loss}} \\ &\cdot\left(1-|S_{22}|^2-|S_{12}|^2-|S_{32}|^2-|S_{42}|^2\right).\end{aligned} \tag{12}$$

Fig. 21 shows the simulation results for the radiation efficiency (η_r) and total efficiency (η_{total}) for the proposed antenna. In either case of Σ-port or Δ-port excitation, the radiation efficiency is about 80% for the antenna in the operation band. The total efficiency, which accounts for the reflection loss and the absorption loss in the termination load, is about 20% lower than the radiation efficiencies. The simulated total efficiency (η_{total}) agrees with the leakage efficiency ($\eta_{leakage}$).

5 Discussion

Table 2 illustrates a comparison between the proposed array of two LWAs with different periods and published LWAs. Most of the SIW periodic LWAs (Liu et al., 2018; Zhou et al., 2018; Ranjan and Ghosh, 2019) were designed to produce a narrow single-beam scanning with frequency. In these single beam scanning periodic LWAs, the scanning continuity usually encounters a stopband at broadside, where the gain drops dramatically and the reflection coefficient increases. In the periodic LWAs with slots, the stopbands were suppressed by reflection elimination (Liu et al., 2018) and impedance matching (Zhou et al., 2018; Ranjan and Ghosh, 2019). Singh and Paras (2022) proposed a dual-beam scanning LWA, which covers all four quadrants of the elevation plane (x-z plane). In other works, some multibeam LWAs were proposed (Geng et al., 2018; Montaseri and Mallahzadeh, 2020; Rahimi et al., 2021), in which the multiple beams were produced based on the radiation from several different-order space harmonics (Montaseri and Mallahzadeh, 2020; Rahimi et al., 2021) or different periodic modulations (Geng et al., 2018). In addition, Geng et al. (2018) used multiple beams in their work to realize beamforming. In Huang and Liu (2022), a null frequency scanning LWA was proposed, which reveals the possibility for an LWA to realize a difference radiation pattern. However, no LWA with different periods has been found that can generate a sum beam and a difference beam simultaneously until now. The LWA array proposed in this paper, in which the two LWAs are with two different periods, can generate a sum beam and a difference beam by an in-phase feed and an out-of-phase feed, respectively.

6 Conclusions

In this paper, we have proposed an array of two periodic LWAs with different periods and integrated with a wideband 180° hybrid. With the Σ-port excited, the array generates a sum beam scanning with

Table 2 Comparison with published leaky-wave antennas

Antenna	ε_r	Operation band (GHz)	Scanning range (measured from broadside direction)	Maximum gain (dBi)	Function
SIW LWA with dual non-identical slots (Liu et al., 2018)	10.2	11–16	−78° to 46.5°	13.86	Single-beam scanning and suppression of open stopband
SIW LWA with transverse slots and vias (Zhou et al., 2018)	10.2	13.2–15.6	−61° to 42°	14.1	Single-beam scanning and suppression of open stopband
SIW LWA with longitude slots and vias (Ranjan and Ghosh, 2019)	3.66	10–17.5	−49° to 69°	17.5	Single-beam scanning and mitigation of open stopband
SIW LWA with transverse and longitude slots (Singh and Paras, 2022)	10.5	11.5–15.5	180° upper space, 180° lower space	13.0	Dual-beam scanning
SIW LWA with transverse slots (Rahimi et al., 2021)	2.94	29.6–36.8	−32° to 59°($n=-1$), −21° to 13°($n=-2$), −84° to −31° ($n=-3$)	15.8 ($n=-1$), 12.7 ($n=-2$), 8 ($n=-3$)	Multibeam scanning
Modulated reactance surfaces LWA (Montaseri and Mallahzadeh, 2020)	3.38	12–18	−1° to 45° ($n=-2$), −37.2° to 17.5°($n=-3$)	4.9 ($n=-1$), 20.6 ($n=-2$), 20.8 ($n=-3$), 7.6 ($n=-4$)	Multibeam scanning
SIW LWA with superposted cosine-shaped slots (Geng et al., 2018)	3.0	16.5–18.5	–	7.5	Multibeam for beamforming
Microstrip periodic LWA with two sets of stubs of different periods (Huang and Liu, 2022)	10.2	9.9–13.8	−38° to 40° (null)	8.9	Null scanning
LWA array of two different periods integrated with 180° hybrid in this paper (in Fig. 10)	2.2	11–17	−33.4° to 20.8° (sum beam), −33.0° to 22.0° (null)	15.9 (sum beam)	Sum and difference beam scanning

SIW: substrate-integrated waveguide; LWA: leaky-wave antenna

frequency. On the other side, with the Δ-port excited, the array generates a difference beam, in which the null occurs between the two beams. The simulation and measurement results were in good agreement and demonstrated that the proposed array has an excellent performance. The sum beam can reach up to 15.9 dBi and can scan from −33.4° to 20.8°. The lowest null depth is −40.8 dB and the angle of the null is almost consistent with the radiation direction of the sum beam. The array of LWAs, which has functionality of sum and difference beam scanning, can be applied in monopulse radar for searching and tracking.

Contributors

Juhua LIU designed the research. Mianfeng HUANG and Juhua LIU processed the data. Mianfeng HUANG drafted the paper. Juhua LIU helped organize the paper. Mianfeng HUANG and Juhua LIU revised and finalized the paper.

Compliance with ethics guidelines

Mianfeng HUANG and Juhua LIU declare that they have no conflict of interest.

Data availability

The data that support the findings of this study are available from the corresponding author upon reasonable request.

References

Bialkowski ME, Wang YF, 2010. Wideband microstrip 180° hybrid utilizing ground slots. *IEEE Microw Wirel Compon Lett*, 20(9):495-497. https://doi.org/10.1109/LMWC.2010.2056677

Geng YJ, Wang JH, Li YJ, et al., 2018. New design of beam-formed leaky-wave antenna based on substrate integrated waveguide in a confined space. *IEEE Trans Antenn Propag*, 66(11):6334-6339. https://doi.org/10.1109/TAP.2018.2867018

Gil-Martínez A, Poveda-García M, García-Fernández J, et al., 2022a. Direction finding of RFID tags in UHF band using a passive beam-scanning leaky-wave antenna. *IEEE J Radio Freq Identif*, 6:552-563. https://doi.org/10.1109/JRFID.2022.3180285

Gil-Martínez A, Poveda-García M, Cañete-Rebenaque D, et al., 2022b. Frequency-scanned monopulse antenna for

RSSI-based direction finding of UHF RFID tags. *IEEE Antenn Wirel Propag Lett*, 21(1):158-162. https://doi.org/10.1109/LAWP.2021.3122233

Gil-Martínez A, Poveda-García M, López-Pastor JA, et al., 2022c. Wi-Fi direction finding with frequency-scanned antenna and channel-hopping scheme. *IEEE Sens J*, 22(6):5210-5222. https://doi.org/10.1109/JSEN.2021.3122232

Gómez-Tornero JL, 2022. Smart leaky-wave antennas for iridescent IoT wireless networks. In: Guo YJ, Ziolkowski RW (Eds.), Antenna and Array Technologies for Future Wireless Ecosystems. Institute of Electrical and Electronics Engineers, Inc., Piscataway, USA, p.119-181. https://doi.org/10.1002/9781119813910.ch4

Hansen RC, 2009. Phased Array Antennas (2nd Ed.). John Wiley & Sons, Inc., Hoboken, USA. https://doi.org/10.1002/9780470529188

Hansen WW, 1946. Radiating Electromagnetic Wave Guide. US Patent 2402622.

Huang MF, Liu JH, 2022. A null frequency scanning leaky-wave antenna. *IEEE Trans Antenn Propag*, 70(9):7625-7635. https://doi.org/10.1109/TAP.2022.3167723

Kim SG, Chang K, 2003. Low-cost monopulse antenna using bi-directionally-fed microstrip patch array. *Electron Lett*, 39(20):1428-1429. https://doi.org/10.1049/el:20030963

Li YJ, Wang JH, 2018. Dual-band leaky-wave antenna based on dual-mode composite microstrip line for microwave and millimeter-wave applications. *IEEE Trans Antenn Propag*, 66(4):1660-1668. https://doi.org/10.1109/TAP.2018.2800705

Li YX, Xue Q, Yung EKN, et al., 2010. The periodic half-width microstrip leaky-wave antenna with a backward to forward scanning capability. *IEEE Trans Antenn Propag*, 58(3):963-966. https://doi.org/10.1109/TAP.2009.2039304

Liu JH, 2021. Periodic leaky-wave antennas based on microstrip-fed slot array with different profile modulations for suppressing open stopband and $n=-2$ space harmonic. *IEEE Trans Antenn Propag*, 69(11):7364-7376. https://doi.org/10.1109/TAP.2021.3078525

Liu JH, Jackson DR, Long YL, 2011. Modal analysis of dielectric-filled rectangular waveguide with transverse slots. *IEEE Trans Antenn Propag*, 59(9):3194-3203. https://doi.org/10.1109/TAP.2011.2161444

Liu JH, Jackson DR, Long YL, 2012. Substrate integrated waveguide (SIW) leaky-wave antenna with transverse slots. *IEEE Trans Antenn Propag*, 60(1):20-29. https://doi.org/10.1109/TAP.2011.2167910

Liu JH, Zhou WL, Long YL, 2018. A simple technique for open-stopband suppression in periodic leaky-wave antennas using two nonidentical elements per unit cell. *IEEE Trans Antenn Propag*, 66(6):2741-2751. https://doi.org/10.1109/TAP.2018.2819701

Mailloux R, 2018. Phased Array Antenna Handbook (3rd Ed.). Artech House, Boston, USA.

Menzel W, 1978. A new travelling wave antenna in microstrip. Proc 8th European Microwave Conf, p.302-306. https://doi.org/10.1109/EUMA.1978.332503

Milligan TA, 2005. Modern Antenna Design (2nd Ed.). John Wiley & Sons, Inc., Hoboken, USA. https://doi.org/10.1002/0471720615

Montaseri N, Mallahzadeh A, 2020. Modulated reactance surfaces with several modulation indices for multi-beam leaky-wave antenna design. *IEEE Trans Antenn Propag*, 68(12):8156-8161. https://doi.org/10.1109/TAP.2020.2996910

Oliner AA, Jackson DR, 2007. Leaky-wave antennas. In: Volakis JL (Ed.), Antenna Engineering Handbook (4th Ed.). McGraw-Hill, New York, USA, p.11-2-11-12.

Pan YS, Cheng Y, Dong YD, 2022. Surface plasmon polariton leaky-wave antennas with wideband arbitrary multi-beam radiation. *IEEE Trans Antenn Propag*, 70(2):931-942. https://doi.org/10.1109/TAP.2021.3111210

Paulotto S, Baccarelli P, Frezza F, et al., 2009. A novel technique for open-stopband suppression in 1-D periodic printed leaky-wave antennas. *IEEE Trans Antenn Propag*, 57(7):1894-1906. https://doi.org/10.1109/TAP.2009.2019900

Poveda-García M, Gómez-Tornero JL, 2021. Ambiguity resolution in amplitude-monopulse systems using broad-beam patterns. *IEEE Antenn Wirel Propag Lett*, 20(4):503-507. https://doi.org/10.1109/LAWP.2021.3055275

Poveda-García M, Cañete-Rebenaque D, Gómez-Tornero JL, 2019. Frequency-scanned monopulse pattern synthesis using leaky-wave antennas for enhanced power-based direction-of-arrival estimation. *IEEE Trans Antenn Propag*, 67(11):7071-7086. https://doi.org/10.1109/TAP.2019.2925970

Poveda-García M, Gómez-Alcaraz A, Cañete-Rebenaque D, et al., 2020. RSSI-based direction-of-departure estimation in Bluetooth low energy using an array of frequency-steered leaky-wave antennas. *IEEE Access*, 8:9380-9394. https://doi.org/10.1109/ACCESS.2020.2965233

Pozar DM, 2011. Microwave Engineering (4th Ed.). John Wiley & Sons, Inc., New York, USA.

Rahimi MR, Sharawi MS, Wu K, 2021. Higher-order space harmonics in substrate integrated waveguide leaky-wave antennas. *IEEE Trans Antenn Propag*, 69(8):4332-4346. https://doi.org/10.1109/TAP.2020.3048530

Ranjan R, Ghosh J, 2019. SIW-based leaky-wave antenna supporting wide range of beam scanning through broadside. *IEEE Antenn Wirel Propag Lett*, 18(4):606-610. https://doi.org/10.1109/LAWP.2019.2897836

Sarkar A, Naqvi AH, Lim S, 2020. (40 to 65) GHz higher order mode microstrip-based dual band dual beam tunable leaky-wave antenna for millimeter wave applications. *IEEE Trans Antenn Propag*, 68(11):7255-7265. https://doi.org/10.1109/TAP.2020.2995430

Scherr S, Ayhan S, Adamiuk G, et al., 2014. Ultrawide bandwidth 180°-hybrid-coupler in planar technology. *Int J Microw Sci Technol*, 2014:486051. https://doi.org/10.1155/2014/486051

Singh AK, Paras N, 2022. A dual-beam steering one dimensional periodic leaky-wave antenna for large coverage. *AEU-Int J Electron Commun*, 145:154086. https://doi.org/10.1016/j.aeue.2021.154086

Tamura J, Arai H, 2022. Angle-of-arrival estimation using null-steering antennas for simplicity and accuracy enhancement. IEEE Int Symp on Antennas and Propagation and USNC-URSI Radio Science Meeting, p.415-416. https://doi.org/10.1109/AP-S/USNC-URSI47032.2022.9886859

Topak E, Hasch J, Wagner C, et al., 2013. A novel millimeter-wave dual-fed phased array for beam steering. *IEEE Trans Microw Theory Tech*, 61(8):3140-3147. https://doi.org/10.1109/TMTT.2013.2267935

Williams JT, Baccarelli P, Paulotto S, et al., 2013. 1-D combline leaky-wave antenna with the open-stopband suppressed: design considerations and comparisons with measurements. *IEEE Trans Antenn Propag*, 61(9):4484-4492. https://doi.org/10.1109/TAP.2013.2271234

Xu SD, Guan DF, Zhang QF, et al., 2019. A wide-angle narrowband leaky-wave antenna based on substrate integrated waveguide-spoof surface plasmon polariton structure. *IEEE Antenn Wirel Propag Lett*, 18(7):1386-1389. https://doi.org/10.1109/LAWP.2019.2917561

Zhang CH, Ren J, Du XY, et al., 2021. Dual-beam leaky-wave antenna based on dual-mode spoof surface plasmon polaritons. *IEEE Antenn Wirel Propag Lett*, 20(10):2008-2012. https://doi.org/10.1109/LAWP.2021.3102060

Zhang QL, Zhang QF, Liu HW, et al., 2019. Dual-band and dual-polarized leaky-wave antenna based on slotted SIW. *IEEE Antenn Wirel Propag Lett*, 18(3):507-511. https://doi.org/10.1109/LAWP.2019.2895339

Zhou WL, Liu JH, Long YL, 2018. Investigation of shorting vias for suppressing the open stopband in an SIW periodic leaky-wave structure. *IEEE Trans Microw Theory Tech*, 66(6):2936-2945. https://doi.org/10.1109/TMTT.2018.2818140

Zhou WL, Liu JH, Long YL, 2019. Applications of the open-stopband suppression in various periodic leaky-wave antennas with tapered half-wavelength line. *IEEE Trans Antenn Propag*, 67(11):6811-6820. https://doi.org/10.1109/TAP.2019.2925192